

# Post-buckling behavior of lattice core sandwich cylindrical shell with functionally graded graphene platelets reinforced face layer resting on elastic foundation

Hakan Çağlar<sup>1</sup>, Arzu Çağlar<sup>2</sup>, Alireza Ataei<sup>\*3</sup>, Rohollah Salmani<sup>4</sup>, Amir Efkar<sup>\*\*5</sup>

<sup>1</sup>Faculty of Engineering and Architecture, Department of Civil Engineering, Kırşehir Ahi Evran University, Kırşehir, Turkey

<sup>2</sup>Faculty of Engineering and Architecture, Department of Architecture, Kırşehir Ahi Evran University, Kırşehir, Turkey

<sup>3</sup>Department of Mathematics, Faculty of Intelligent Systems Engineering and Data Science, Persian Gulf University, Bushehr, 75169, Iran

<sup>4</sup>Department of Mechanical Engineering, Lahijan Branch, Islamic Azad University, Lahijan, Iran

<sup>5</sup>School of Mechanical Engineering, College of Engineering, University of Tehran, Tehran, Iran

(Received October 31, 2022, Revised November 4, 2024, Accepted January 16, 2025)

**Abstract.** This paper presents the buckling and post-buckling behavior of a sandwich shell with a lattice polymer core and nanocomposite face layer reinforced with graphene platelets. The rule of mixtures is used to determine the effective mechanical properties of graphene platelet-reinforced surfaces at different distributions along the thickness. The governing deflection equations are derived using high-order shear deformation theory and consider the effects of large deformations with nonlinear von Karman strain-displacement relationships. The elastic foundation is modeled using a two-parameter model developed by Winkler-Pasternak. A closed-form solution method utilizing the Ritz energy approach and Airy stress function is employed for solving nonlinear equations and identifying post-buckling paths under external mechanical forces, including radial compression and axial force. Method validation involves comparison with prior studies' results. The analytical solution explores various parameters, including graphene platelet volume fraction, distribution, lattice core geometric characteristics, and elastic substrate properties, on the buckling and post-buckling behavior of the cylindrical shell. Results indicate that, under axial compression, a moderately long cylindrical shell shows a snap-through equilibrium path after buckling.

**Keywords:** analytical solution; graphene platelets reinforcement; high-order shear theory; lattice core; post-buckling; sandwich shell

## 1. Introduction

The growing demand for advancements in science and technology has intensified the need for lightweight, low-density structures, particularly in sectors like aerospace, automotive, marine, and military applications. Sandwich and composites structures featuring diverse core configurations are favored for their low weight-to-area ratio, impressive strength, stiffness, and ability to absorb impact energy, making them ideal for crashworthy applications (Faraji *et al.* 2023, Boroujeni *et al.* 2024). Among these, auxetic cellular solid structures are particularly noteworthy due to their unique mechanical properties; they expand laterally when stretched and contract when compressed, exhibiting anti-rubber behavior. These structures possess superior mechanical characteristics, including (a) resistance to indentation, (b) enhanced fracture toughness, and (c) higher shear modulus compared to traditional materials. As a result of these exceptional properties, lattice structures are increasingly utilized as cores in a variety of sandwich constructions, including sheets, shells, and cylinders.

Auxetic materials, which exhibit a negative Poisson's ratio, have gained significant attention due to their unique mechanical properties (Wojciechowski and Branca 1989). These structures expand laterally when stretched, contrary to conventional materials. In foundational studies, Wojciechowski *et al.* (1987, 1989) demonstrated that a dense thermodynamically stable phase formed by hard cyclic hexamers exhibits NPR through Monte Carlo simulations. This model was later generalized for static analysis. Lakes (1991) introduced the hexa-chiral structure, a simplification of the hard hexamer model, where intermolecular interactions are reduced and replaced with elastic ribs, allowing for the exploration of negative Poisson's ratio in engineered designs. By manipulating the arrangement of these structures, it is possible to achieve configurations that maintain negative Poisson's ratio characteristics. Recent studies have demonstrated that the presence of disorder, such as size dispersion of nodes, can significantly affect the Poisson's ratio and the overall mechanical behavior of auxetic structures. For instance, Pozniak and Wojciechowski (2014) highlighted how variations in node sizes within the anti-tetra-chiral configuration influenced deformation characteristics and led to altered mechanical responses. This insight emphasizes the need for further investigation into how size distribution impacts the mechanical properties of nanocomposite materials and their design implications. Surprising behavior of strongly auxetic plates was observed by Streck *et al.*

\*Corresponding author, Ph.D.,

E-mail: ataei@pgu.ac.ir

\*\*Co-corresponding author, Ph.D.,

E-mail: afker@ut.ac.ir

(2014) and Pozniak *et al.* (2013).

Numerous studies have explored the bending and vibration behavior of sandwich structures featuring lattice metamaterial cores (Toygar *et al.* 2016, Soleimani-Javid *et al.* 2022, Celiktas *et al.* 2019, Kolahdouzan *et al.* 2022). Shah *et al.* (2022) investigated the dynamic response of sandwich plates with a honeycomb core by finite element technique. Khosravi *et al.* (2021) development a seismic fragility curves of cylindrical concrete tanks using nonlinear analysis. Duc *et al.* (2017) investigated the dynamic behavior and vibration characteristics of negative Poisson ratios double-curved shallow shells, featuring honeycomb core layers supported on foundations, subjected to blast and damping loads. Based on full-scale finite element simulations in three dimensions, Li *et al.* (2019) examined the thermal post-buckling response of the beam in the large deflection area and the variation of the effective Poisson's ratio. Karnesis and Burriesci (2013), along with Scarpa *et al.* (2008), examined the global buckling behavior of auxetic cellular tubes featuring inverted hexagonal honeycomb structures. Their findings indicate that the integration of auxetic structures can substantially enhance the buckling performance of cellular tubes, outperforming traditional non-auxetic designs. This improvement is attributed to the unique mechanical properties of auxetic materials, which exhibit a negative Poisson's ratio. When subjected to axial loads, auxetic structures tend to expand laterally instead of contracting, which provides better energy absorption and load distribution characteristics. Quang *et al.* (2022) present a study of nonlinear buckling of a magneto-electro-elastic plate on an elastic foundation. An analysis of the post-buckling performance of sandwich plates with functionally graded (FG) auxetic 3D lattice cores was proposed by Li *et al.* (2020). Lim (2014a, b) also examined the buckling performance of quadrilateral and circular thick auxetic plates to discuss the potential applications of the auxetic plate and shell. Zhang *et al.* (2016) demonstrated that auxetic materials significantly improve the buckling capacity of rectangular plates subjected to uniaxial compression. Their research highlights how the unique mechanical behavior of auxetic materials, characterized by a negative Poisson's ratio, allows these plates to better withstand compressive forces. Unlike traditional materials that contract laterally when compressed, auxetic materials expand, distributing stress more effectively across the plate. This leads to an increased critical buckling load, allowing for greater structural integrity and performance. The findings from this study emphasize the potential of integrating auxetic materials into engineering designs, particularly in applications where enhanced stability and load-bearing capabilities are essential. In Li *et al.* (2022) experiment, cylinder-shaped sandwich shells with a 3D triple-V metalattice core and graphene-reinforced composite facesheet were tested for post-buckling behavior. Thermal surroundings, strut radius, shell length, and curvature radius are also deliberated in detail.

Nanomaterials are materials with structural features at the nanoscale. At this scale, materials exhibit unique physical, chemical, and biological properties that differ

significantly from their bulk counterparts (Rostami *et al.* 2024, Faraji *et al.* 2023). There is a novel generation of composite materials, mentioned to as nanocomposite materials, in which the microstructural specifics are different spatially (Rezaee and Maleki 2015, Pourreza *et al.* 2021, Akbarzadeh *et al.* 2022, An *et al.* 2024). It is essential to strengthen materials mechanical characteristics and use composite materials due to the low strength and low thermal resistance of polymers as opposed to other materials (Pourreza *et al.* 2022, Faraji *et al.* 2023, Boroujeni *et al.* 2024). Therefore, many researchers and engineers have conducted extensive research on polymer nanocomposites. A small percentage of nanoparticles added to polymers significantly increases their mechanical, thermal, electrical, and magnetic properties (Hao *et al.* 2024). Due to their high mechanical strength, corrosion resistance, low production costs, ease of processing, and lightness, polymer composites reinforced with nanoparticles are suitable alternatives to metal and ceramic structures (Bhandari, 2019).

The mechanical characteristics and buckling behavior of composites reinforced with nanoparticles have been considered by various researchers using analytical and experimental approaches. Using the finite element numerical method, Li *et al.* (2014) examined the buckling performance of cylinder-shaped shells reinforced with carbon nanotubes in dissimilar arrangements. Mori-Tanaka approach was applied to obtain equivalent properties. The buckling of a three-layer cylindrical shell reinforced with graphene nanosheets was examined by Feng *et al.* (2017) for both FG and uniform distribution modes of graphene nanosheets. To determine the properties of nanocomposite materials, they used molecular dynamics results and laws of mixtures. Using Hamilton's principle, the equations of motion for the cylindrical shell were derived. Hamilton's principle, which states that the actual motion of a system is such that it minimizes the action integral, provides a powerful framework for formulating the equations of motion.

Javani *et al.* (2021) examined the nonlinear buckling performance of multilayer combined polymer plates strengthened with GPLs under plate loads and during the buckling and post-buckling process. By considering nonlinear von-Karman relations, they included large deformations in the equations and derived the nonlinear coupling equations governing the system using differential changes and Lagrange equations. Torbati *et al.* (2019) conducted a numerical study on the buckling behavior of carbon nanotube-reinforced composite plates subjected to thermal loads, employing high-order shear deformation theories. Their research aimed to analyze how thermal effects influence the stability of these composite structures, particularly focusing on the role of carbon nanotubes in enhancing mechanical properties. By utilizing high-order shear theories, which account for transverse shear deformations more accurately than traditional theories, the study provided a detailed understanding of the critical buckling loads and deformation patterns of the plates. Abdanak *et al.* (2018) considered the influence of functionalized GPLs on the bending behavior of an epoxy/basalt fiber composite. A nanocomposite containing

4% GPLs by weight increased its flexural strength, flexural modulus, and fracture energy by 89.6%, 252.6%, and 44.6%, respectively, over the base sample.

Numerous studies have focused on exploring the mechanical behavior of beams, sheets, and panels composed of functionally graded nanocomposites and lattice cores (Jahanghiry *et al.* 2016, Karami *et al.* 2019, Wu *et al.* 2019). However, very few works have been conducted on the buckling behavior of cylindrical shells composed of FG nanocomposites face layer and lattice core. To date, there has been no investigation into the buckling and post-buckling behavior of cylindrical shells featuring lattice cores and surface layers strengthened with GPLs. This research aims to address this gap by examining the nonlinear buckling and post-buckling characteristics of a sandwich shell composed of a mesh core and a GPL-reinforced nanocomposite surface layer, supported on a Winkler-Pasternak elastic substrate. The study will utilize the Ritz energy method to derive an analytical solution, formulating the governing nonlinear equations based on high-order shear deformation theory.

The organization of this paper is as follows. Section 2 outlines the governing equations used in this study, detailing the mechanical characteristics of both the nanocomposite surface layer and the lattice core, followed by the stress-strain relations. Section 3 discusses the methodology for solving these equations. In Section 4, we present and discuss the results, including verification of results, nonlinear buckling behavior, and post-buckling behavior. Finally, Section 5 concludes the paper by summarizing key findings and potential directions for future research.

## 2. Governing equations

Fig. 1 shows the geometric features of the FG sandwich cylinder-shaped shell with lattice core based on the Winkler-Pasternak elastic bed. The shell has the following geometric dimensions: distance of  $L$ , the radius of  $R$ , the core thickness of  $h_c$ , and the surface thickness of  $h_s$ . To derive the equations, we used a Cartesian coordinate  $(x, y, z)$  whose origin is positioned in the middle plane. The elastic foundation is demonstrated using Winkler's spring and Pasternak's shear models. Along the thickness of the shell, the mechanical properties of the internal and external surfaces change gradually.

### 2.1 Mechanical characteristic of nanocomposite surface layer

In the current research, the surface layer is functionally reinforced by GPLs. This study assumes that all samples have the same total mass of GPLs, and total volume fraction remains  $V_{GPL}^*$ . The volume fraction can be calculated using the following equation:

$$V_{GPL}^* = \frac{W_{GPL}}{W_{GPL} + \left(\frac{\rho_{GPL}}{\rho_m}\right) - \left(\frac{\rho_{GPL}}{\rho_m}\right) W_{GPL}} \quad (1)$$

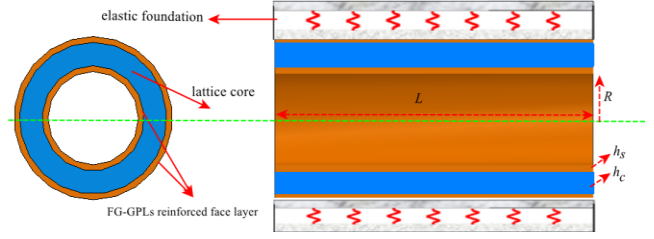


Fig. 1 Cylindrical sandwich shell geometry with lattice core and GPLs reinforced face layer with different distributions of GPLs located on Winkler-Pasternak elastic substrate

where  $W_{GPL}$  is a function of the mass of GPLs,  $\rho_{GPL}$  and  $\rho_m$  remain the density of GPLs and polymer, respectively. In this research, three different kinds of GPLs distribution along the width of the surface layers are investigated; under the title of GPL-U (uniform distribution), GPL-S (symmetric distribution) and GPL-A (asymmetric distribution). In this case, the volume fraction in the surface layers reinforced with GPLs is obtained as a functional scale as follows (Shi *et al.* 2017):

For type GPL-U (uniform distribution):

$$V_{GPL} = V_{GPL}^* \quad (2)$$

For GPL-S (symmetric distribution):

$$V_{GPL} = V_{GPL}^* \left[ 1 - \cos\left(\frac{\pi z}{h}\right) \right] \quad (3a)$$

For GPL-A (asymmetric distribution):

$$V_{GPL} = V_{GPL}^* \left[ 1 - \cos\left(\frac{\pi z}{h} + \frac{\pi}{4}\right) \right] \quad (3b)$$

The effective mechanical properties of surface reinforced with GPL, such as Young's, shear modulus, and Poisson's ratio, can be determined using rule of mixtures. These properties are expressed as follows (Shi *et al.* 2017):

$$E_x = \eta_1 V_{GPL} E_x^{GPL} + V_m E^m \quad (4)$$

$$\frac{\eta_2}{E_y} = \frac{V_{GPL}}{E_y^{GPL}} + \frac{V_m}{E^m} \quad (5)$$

$$\frac{\eta_3}{G_{xy}} = \frac{V_{GPL}}{G_{xy}^{GPL}} + \frac{V_m}{G^m} \quad (6)$$

$$V_{GPL} + V_m = 1 \quad (7)$$

$$\nu_{xy} = V_{GPL} \nu_{xy}^{GPL} + V_m \nu^m \quad (8)$$

$$\nu_{xy} = \frac{\nu_{xy}}{E_x} E_y \quad (9)$$

$$\rho = V_{GPL} \rho^{GPL} + V_m \rho^m \quad (10)$$

where,  $E_x^{GPL}$ ,  $E_y^{GPL}$ , and  $G_{xy}^{GPL}$  represents elastic modulus in longitudinal and transverse direction, and the shear modulus, respectively.  $E^m$  and  $G^m$  represent elastic and shear modulus of the matrix, respectively.  $\nu^{GPL}$  and  $\rho^{GPL}$  are Poisson's ratio and the density of GPLs.  $\rho^m$  and  $\nu^m$  are the density and Poisson's ratio of the matrix, respectively.

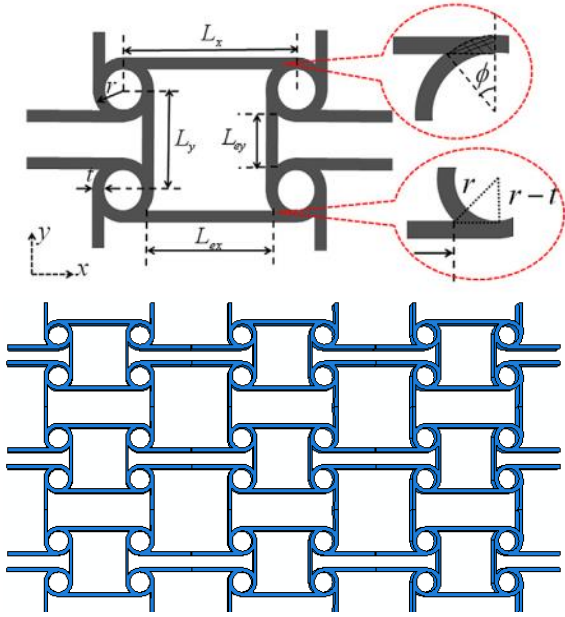


Fig. 2 Geometry of the anti-tetrachiral anisotropic cell

### 2.3 Mechanical characteristics of lattice core

To obtain the governing equations, the high-order shear deformation theory is used for cylindrical shells. For cylindrical shells, the nonlinear displacement fields are as follows:

$$\begin{aligned} u_x &= u - zw_{,x} + g(z)[\Phi_x(x, y) + w_{,x}] \\ u_y &= \left(1 + \frac{z}{R}\right)v - zw_{,y} + g(z)[\Phi_y(x, y) + w_{,y}] \\ u_z &= w(x, y) \end{aligned} \quad (13)$$

in which  $u$ ,  $v$  and  $w$  are the displacement components of the middle plane of the shell in the  $x$ -,  $y$ - and  $z$ - directions, respectively.  $\Phi_x$  and  $\Phi_y$  denote the rotations of the normal transverse vector around the  $y$ - and  $x$ -axes, respectively.

The von Karman nonlinear strain-displacement relations used in this study are essential for accurately modeling the geometric nonlinearity of cylindrical shells during significant deformations. These relations effectively capture the mid-plane strain components and allow for a comprehensive analysis of both buckling and post-buckling behavior, ensuring the results are reliable under the specific loading conditions examined.

Using the Von-Karman nonlinear strain-displacement relations for cylinder-shaped shells, the mid-plane strain components can be detailed as follows: (Kim and Reddy 2015):

$$\boldsymbol{\varepsilon} = \begin{Bmatrix} \varepsilon_x \\ \varepsilon_y \\ \varepsilon_{xy} \end{Bmatrix} = \begin{Bmatrix} u_{,x} + \frac{1}{2}w_{,x}^2 \\ \left(\frac{1}{1 + \frac{z}{R}}\right)\left(v_{,y} + \frac{w}{R}\right) - \frac{1}{2\left(1 + \frac{z}{R}\right)^2}w_{,y}^2 \\ \left(\frac{1}{1 + \frac{z}{R}}\right)u_{,y} + v_{,x} - w_{,x}w_{,y} \end{Bmatrix} \quad (14)$$

The strain components in the thickness at the position of the  $z$  in shell thickness are obtained as follows:

$$\begin{aligned} \varepsilon_x &= \varepsilon_x^0 + z\chi_x^{(0)} + g(z)\chi_x^{(2)}, \\ \varepsilon_y &= \varepsilon_y^0 + z\chi_y^{(0)} + g(z)\chi_y^{(2)}, \quad \gamma_{xy} = g(z)z\chi_{xy}^{(1)} \end{aligned} \quad (15)$$

where in

$$\begin{aligned} \boldsymbol{\varepsilon}^0 &= \begin{Bmatrix} \varepsilon_x^{(0)} \\ \varepsilon_y^{(0)} \\ \varepsilon_{xy}^{(0)} \end{Bmatrix} = \begin{Bmatrix} u_{,x} + \frac{1}{2}w_{,x}^2 \\ v_{,y} + \frac{w}{R} + \frac{1}{2}w_{,y}^2 \\ u_{,y} + v_{,x} + w_{,x}w_{,y} \end{Bmatrix}, \\ \boldsymbol{\chi}^{(0)} &= \begin{Bmatrix} \chi_x^{(0)} \\ \chi_y^{(0)} \\ \chi_{xy}^{(0)} \end{Bmatrix} = \begin{Bmatrix} -w_{,xx} \\ w_{,yy} \\ 2w_{,xy} \end{Bmatrix}, \\ \boldsymbol{\chi}^{(2)} &= \begin{Bmatrix} \chi_x^{(2)} \\ \chi_y^{(2)} \\ \chi_{xy}^{(2)} \end{Bmatrix} = \begin{Bmatrix} \Phi_{x,x} + w_{,xx} \\ \Phi_{y,y} + w_{,yy} \\ \Phi_{x,y} + \Phi_{y,x} + 2w_{,xy} \end{Bmatrix} \end{aligned} \quad (16)$$

and

$$\chi_{xy}^{(1)} = \Phi_{x,y} + w_{,x} \quad (17)$$

### 2.4 Stress-strain relations

According to Hooke's stress-strain relations, the structural equations for the core section and the surface layer of the cylindrical shell are as follows (Reddy 2003):

$$\begin{aligned} \boldsymbol{\sigma}^{(c)} &= \begin{Bmatrix} \sigma_x \\ \sigma_y \\ \tau_{xy} \end{Bmatrix} = \mathbf{K}^{(c)} \boldsymbol{\varepsilon} = \begin{bmatrix} C_{11} & C_{12} & 0 \\ C_{21} & C_{22} & 0 \\ 0 & 0 & C_{66} \end{bmatrix}_{(c)} \begin{Bmatrix} \varepsilon_x \\ \varepsilon_y \\ \gamma_{xy} \end{Bmatrix}, \\ \boldsymbol{\sigma}^{(f)} &= \begin{Bmatrix} \sigma_x \\ \sigma_y \\ \tau_{xy} \end{Bmatrix} = \mathbf{K}^{(f)} \boldsymbol{\varepsilon} = \begin{bmatrix} C_{11} & C_{12} & 0 \\ C_{21} & C_{22} & 0 \\ 0 & 0 & C_{66} \end{bmatrix}_{(f)} \begin{Bmatrix} \varepsilon_x \\ \varepsilon_y \\ \gamma_{xy} \end{Bmatrix} \end{aligned} \quad (18)$$

and

$$\begin{aligned} \begin{Bmatrix} \varepsilon_x \\ \varepsilon_y \\ \gamma_{xy} \end{Bmatrix} &= \begin{bmatrix} \frac{1}{E_x} & -\frac{\nu_{xy}}{E_y} & 0 \\ -\frac{\nu_{xy}}{E_x} & \frac{1}{E_x} & 0 \\ 0 & 0 & \frac{1}{G_{xy}} \end{bmatrix}_{(c)} \begin{Bmatrix} \sigma_x \\ \sigma_y \\ \tau_{xy} \end{Bmatrix}, \\ \begin{Bmatrix} \varepsilon_x \\ \varepsilon_y \\ \gamma_{xy} \end{Bmatrix} &= \begin{bmatrix} \frac{1}{E_x} & -\frac{\nu_{xy}}{E_y} & 0 \\ -\frac{\nu_{xy}}{E_x} & \frac{1}{E_x} & 0 \\ 0 & 0 & \frac{1}{G_{xy}} \end{bmatrix}_{(f)} \begin{Bmatrix} \sigma_x \\ \sigma_y \\ \tau_{xy} \end{Bmatrix} \end{aligned} \quad (19)$$

where the indices  $c$  and  $f$  represent the lattice core and nanocomposite layers, respectively. Considering the mechanical properties of each layer, the constants  $C_{ij}$ ,  $i, j = 1..6$  are defined as follows (Reddy 2003):

$$C_{11} = \frac{E_x}{1 - \nu_{xy}\nu_{yx}}, \quad C_{12} = \frac{E_y\nu_{xy}}{1 - \nu_{xy}\nu_{yx}}, \quad (20)$$

$$C_{21} = \frac{E_y \nu_{xy}}{1 - \nu_{xy} \nu_{yx}}, C_{21} = \frac{E_x \nu_{xy}}{1 - \nu_{xy} \nu_{yx}}$$

$$C_{22} = \frac{E_y}{1 - \nu_{xy} \nu_{yx}}, C_{66} = G_{xy}$$

where  $E_x$ ,  $E_y$ ,  $\nu_{xy}$  and  $\nu_{yx}$  respectively represent the elasticity modulus and Poisson's ratio in  $x$ - and  $y$ -directions. For functional graded cylindrical shell  $E_x \nu_{yx} = E_y \nu_{xy}$  and  $G_{xy}$  stands shear modulus.

For thin-walled cylinder-shaped shells ( $\frac{h}{R} \ll 1$ ), the force and stress resultants are fundamental to understanding the structural behavior under various loading conditions. These resultants can be defined as follows:

$$\begin{aligned} & \{(N_x, N_y, N_{xy}), (M_x, M_y, M_{xy})\} \\ &= \int_{-h_c-h_s}^{-h_c} \{\sigma_x, \sigma_y, \sigma_{xy}\}^{(f)}(1, z) dz \\ &+ \int_{-h_c}^{h_c} \{\sigma_x, \sigma_y, \sigma_{xy}\}^{(c)}(1, z) dz \\ &+ \int_{h_c}^{h_c+h_s} \{\sigma_x, \sigma_y, \sigma_{xy}\}^{(f)}(1, z) dz \end{aligned} \quad (21a)$$

As a result, by replacing Eqs. (16)-(19) into Eq. (21a), the resultants of stress applied on the middle-plane are written as:

$$\begin{aligned} \mathbf{N} &= \int_{-h_c-h_s}^{-h_c} \boldsymbol{\sigma}^{(f)}(1, z) dz \\ &+ \int_{-h_c}^{h_c} \boldsymbol{\sigma}^{(c)}(1, z) dz + \int_{h_c}^{h_c+h_s} \boldsymbol{\sigma}^{(f)}(1, z) dz, \\ \mathbf{M} &= \int_{-h_c-h_s}^{-h_c} z \boldsymbol{\sigma}^{(f)}(1, z) dz \\ &+ \int_{-h_c}^{h_c} z \boldsymbol{\sigma}^{(c)}(1, z) dz + \int_{h_c}^{h_c+h_s} z \boldsymbol{\sigma}^{(f)}(1, z) dz, \\ \mathbf{P} &= \int_{-h_c-h_s}^{-h_c} g(z) \boldsymbol{\sigma}^{(f)}(1, z) dz \\ &+ \int_{-h_c}^{h_c} g(z) \boldsymbol{\sigma}^{(c)}(1, z) dz + \int_{h_c}^{h_c+h_s} g(z) \boldsymbol{\sigma}^{(f)}(1, z) dz, \\ \mathbf{R} &= \int_{-h_c-h_s}^{-h_c} g(z) {}_z \boldsymbol{\sigma}^{(f)}(1, z) dz \\ &+ \int_{-h_c}^{h_c} g(z) {}_z \boldsymbol{\sigma}^{(c)}(1, z) dz + \int_{h_c}^{h_c+h_s} g(z) {}_z \boldsymbol{\sigma}^{(f)}(1, z) dz, \end{aligned} \quad (21b)$$

where  $\mathbf{N} = \{N_x, N_y, N_{xy}\}^T$ ,  $\mathbf{M} = \{M_x, M_y, M_{xy}\}^T$ ,  $\mathbf{R} = \{R_x, R_y\}^T$  and  $\mathbf{P} = \{P_x, P_y, P_{xy}\}^T$  respectively represent the resulting vectors of force, moment, high-order, and shear force.

By replacing Eq. (18) in Eq. (21) and using Eq. (14), the relationship between the output amounts and displacements is presented as follows:

$$\begin{Bmatrix} \mathbf{N} \\ \mathbf{M} \\ \mathbf{P} \end{Bmatrix} = \begin{bmatrix} \mathbf{A} & \mathbf{B} & \mathbf{C} \\ \mathbf{B} & \mathbf{D} & \mathbf{E} \\ \mathbf{C} & \mathbf{E} & \mathbf{F} \end{bmatrix} \begin{Bmatrix} \boldsymbol{\varepsilon}^{(0)} \\ \boldsymbol{\chi}^{(0)} \\ \boldsymbol{\chi}^{(2)} \end{Bmatrix}, \mathbf{R} = \mathbf{H} \boldsymbol{\chi}^{(1)} \quad (22a)$$

where the constants of the matrix are stiffness coefficients

and define as follows:

$$\begin{aligned} A_{ij} &= \int_{-h}^h K_{ij} dz, B_{ij} = \int_{-h}^h z K_{ij} dz, \\ C_{ij} &= \int_{-\frac{h}{2}}^{\frac{h}{2}} g(z) K_{ij} dz, \\ D_{ij} &= \int_{-h}^h z^2 K_{ij} dz, E_{ij} = \int_{-h}^h z g(z) K_{ij} dz, \\ F_{ij} &= \int_{-h}^h g^2(z) K_{ij} dz, H_{ij} = \int_{-h}^h z g^2(z) {}_z K_{ij} dz, \end{aligned} \quad (22b)$$

## 2.5 Buckling and post-buckling equations

To develop the equilibrium equations related to buckling and post-buckling of the cylindrical shells under investigation, the virtual work method is used. For static buckling problems, potential energy includes elastic strain energy,  $\Pi_s$ , virtual work thru by external forces,  $\Pi_f$ , and elastic substrate,  $\Pi_e$ . Based on the principle of minimum potential energy, we will have:

$$\delta \int_V (\Pi_s + \Pi_e - \Pi_f) dV = 0 \quad (23)$$

The virtual strain energy of cylindrical shell is obtained as:

$$\begin{aligned} \delta \Pi_s &= \int_0^{2\pi R} \int_0^L \int_{-h}^h (\sigma_x \delta \varepsilon_x + \tau_{xy} \delta \gamma_{xy} \\ &\quad + \sigma_y \delta \varepsilon_y) dx dy dz \\ &= \int_0^{2\pi R} \int_0^L \int_{-h}^h \left( N_x \varepsilon_x^{(0)} + N_y \varepsilon_y^{(0)} + N_{xy} \varepsilon_{xy}^{(0)} \right. \\ &\quad \left. + M_x \chi_x^{(0)} + M_y \chi_y^{(0)} + M_{xy} \chi_{xy}^{(0)} \right. \\ &\quad \left. + P_x \chi_x^{(2)} + P_y \chi_y^{(2)} + P_{xy} \chi_{xy}^{(2)} + R_x \chi_{xy}^{(1)} \right) dx dy dz \end{aligned} \quad (24)$$

Also, the virtual potential energy changes by Winkler-Pasternak nonlinear elastic foundation can be expressed as:

$$\delta \Pi_e = \int_0^{2\pi R} \int_0^L \left( k_w w \delta w + \frac{1}{2} k_p \frac{\partial w}{\partial x} \delta \frac{\partial w}{\partial x} \right) dx dy \quad (25)$$

where  $k_w$  is Winkler foundation stiffness modulus and  $k_p$  is foundation shear stiffness are based on the Pasternak model. It is assumed that the shell is simultaneously affected by uniform radial force  $q$  and mean axial stress of  $\sigma_{ox}$ . In this case, the external force virtual work is obtained as:

$$\begin{aligned} \delta \Pi_f &= -q \int_0^{2\pi R} \int_0^L \delta w dx dy \\ &\quad - \sigma_{ox} h \int_0^{2\pi R} \int_0^L \delta \frac{\partial u}{\partial x} dx dy \end{aligned} \quad (26)$$

By substituting displacement components from Eq. (16) in  $\delta \Pi_f$ , the following equation is obtained:

$$\delta \Pi_f = q \int_0^{2\pi R} \int_0^L (\delta w) dx dy \quad (27)$$

$$-\sigma_{0x} h \int_0^{2\pi R} \int_0^L \left( \delta \varepsilon_x^0 - \frac{\partial(\delta w)}{\partial x} \frac{\partial w}{\partial x} \right) dx dy$$

To derive the nonlinear differential equations governing the buckling and post-buckling behavior of cylindrical shells with a lattice core and reinforced surface layers with GPLs, we first substitute Eqs. (24)-(27) into Eq. (23). Next, we apply integration by parts and organize the coefficients associated with the variables  $\delta u$ ,  $\delta w$ ,  $\delta v$ ,  $\delta \Phi_x$ , and  $\delta \Phi_y$ . we will have:

$$\delta u: \frac{\partial N_x}{\partial x} + \frac{\partial N_{yx}}{\partial y} = 0 \quad (28)$$

$$\delta v: \frac{\partial N_{xy}}{\partial x} + \frac{\partial N_y}{\partial y} = 0 \quad (29)$$

$$\begin{aligned} \delta w: & \frac{\partial^2 M_x}{\partial x^2} + \frac{\partial^2 M_y}{\partial y^2} + 2 \frac{\partial^2 M_{xy}}{\partial x \partial y} + \frac{\partial}{\partial x} \left( N_x \frac{\partial w}{\partial x} + N_{xy} \frac{\partial w}{\partial y} \right) \\ & + \frac{\partial}{\partial y} \left( N_y \frac{\partial w}{\partial y} + N_{xy} \frac{\partial w}{\partial x} \right) - \frac{N_y}{R} - \frac{\partial^2 P_x}{\partial x^2} - \frac{\partial^2 P_y}{\partial y^2} \\ & - 2 \frac{\partial^2 P_{xy}}{\partial x \partial y} + \frac{\partial R_x}{\partial x} + \frac{\partial R_y}{\partial y} - k_w w + k_p \frac{\partial^2 w}{\partial x^2} + k_p \frac{\partial^2 w}{\partial y^2} = q \end{aligned} \quad (30)$$

$$\delta \Phi_x: \frac{\partial P_x}{\partial x} + \frac{\partial P_{xy}}{\partial y} - R_x = 0 \quad (31)$$

$$\delta \Phi_y: \frac{\partial P_y}{\partial y} + \frac{\partial P_{xy}}{\partial x} - R_y = 0 \quad (32)$$

According to the assumptions it can be considered  $u \ll w$ . Based on this, using Eqs. (28) and (29), Airy function,  $\Psi(x, y)$ , defined as:

$$N_x = \Psi_{,yy}, N_y = \Psi_{,xx}, N_{xy} = -\Psi_{,xy} \quad (33)$$

By deriving from  $\varepsilon_x^0$ ,  $\varepsilon_y^0$  and  $\gamma_{xy}^0$  respectively with respect to  $y$ ,  $x$  and  $xy$  the nonlinear equation governing compatibility conditions is obtained as:

$$\varepsilon_{x,yy}^0 + \varepsilon_{y,xx}^0 - \gamma_{xy,xy}^0 = \frac{1}{R} w_{,xx} - w_{,xx} w_{,yy} + (w_{,xy})^2 \quad (34)$$

Considering Eqs (19) and (33) and substituting them into Eq. (34), we derive the compatibility equation, which is crucial for ensuring the consistency between the deformation and stress fields within the structure. The process is outlined as follows:

$$\begin{aligned} & h \left[ A_{10}^* \frac{\partial^4 \Psi}{\partial x^4} + (A_{20}^* + A_{30}^* + A_{50}^*) \frac{\partial^4 \Psi}{\partial x^2 \partial y^2} + A_{40}^* \frac{\partial^4 \Psi}{\partial y^4} \right] \\ & - A_{11}^* \frac{\partial^4 w}{\partial x^4} - (A_{21}^* + A_{31}^* - A_{51}^*) \frac{\partial^4 w}{\partial x^2 \partial y^2} - A_{41}^* \frac{\partial^4 w}{\partial y^4} \\ & = \left( \frac{\partial^2 w}{\partial x \partial y} \right)^2 - \frac{1}{R} \frac{\partial^2 w}{\partial x^2} - \frac{\partial^2 w}{\partial x^2} \frac{\partial^2 w}{\partial y^2} \end{aligned} \quad (35)$$

in which

$$\begin{aligned} A_{10}^* &= \frac{A_{10}}{\Delta}, A_{20}^* = -\frac{A_{20}}{\Delta}, A_{30}^* = -\frac{A_{30}}{\Delta}, A_{51}^* = -\frac{2A_{51}}{A_{50}} \\ A_{40}^* &= \frac{A_{40}}{\Delta}, A_{50}^* = \frac{1}{A_{50}}, A_{11}^* = \frac{A_{11}A_{30} - A_{31}A_{10}}{\Delta} \end{aligned} \quad (36)$$

$$\begin{aligned} A_{21}^* &= \frac{A_{21}A_{30} - A_{41}A_{10}}{\Delta}, A_{31}^* = \frac{A_{31}A_{20} - A_{11}A_{40}}{\Delta} \\ A_{41}^* &= \frac{A_{41}A_{20} - A_{21}A_{40}}{\Delta}, \Delta = A_{10}A_{40} - A_{20}A_{30} \end{aligned}$$

Replacing Eqs. (14), (23) and (33) in Eq. (30) and assuming  $u \ll w$  and  $v \ll w$ , we will have:

$$\begin{aligned} & \left[ B_1^* \frac{\partial^4 \Psi}{\partial x^4} + B_2^* \frac{\partial^4 \Psi}{\partial x^2 \partial y^2} + B_3^* \frac{\partial^4 \Psi}{\partial y^4} \right] \\ & - B_5^* \frac{\partial^4 w}{\partial x^4} - B_5^* \frac{\partial^4 w}{\partial x^2 \partial y^2} - B_6^* \frac{\partial^4 w}{\partial y^4} + \frac{1}{R} \frac{\partial \Psi}{\partial x^2} \\ & + \left[ \frac{\partial^2 w}{\partial x^2} \frac{\partial^2 \Psi}{\partial y^2} - 2 \frac{\partial^2 w}{\partial y \partial x} \frac{\partial^2 \Psi}{\partial y \partial x} + \frac{\partial^2 \Psi}{\partial x^2} \frac{\partial^2 w}{\partial y^2} \right] \\ & - k_w w + k_p \left( \frac{\partial^2 w}{\partial x^2} + \frac{\partial^2 w}{\partial y^2} \right) = 0 \end{aligned} \quad (37)$$

in which

$$\begin{aligned} B_1^* &= A_{11}A_{20}^* + A_{21}A_{10}^*, \\ B_2^* &= A_{40}A_{10}^* - A_{21}A_{30}^* - A_{11}A_{20}^* - A_{21}A_{10}^*, \\ B_3^* &= A_{11}A_{40}^* - A_{21}A_{30}^* \\ B_4^* &= A_{11}A_{20}^* + 2A_{21}A_{10}^* - A_{31}A_{40}^*, \\ B_5^* &= A_{21}A_{10}^* - 2A_{22}A_{31}^* - A_{11}A_{20}^*, \\ B_6^* &= A_{21}A_{10}^* + 2A_{12}A_{10}^* - A_{11}A_{30}^*, \end{aligned} \quad (38)$$

### 3. Solving equations

Assuming  $w(x)$  for the static deformation and placing it in Eq. (35), the Airy function can be calculated. After determining the Airy function and placing it in Eq. (37) and applying the Ritz energy method, the hypothetical response constants can be determined.

To derive the buckling equation for the system, we begin by considering the hypothetical response of the static deformation function. This approach enables us to formulate the governing equations associated with the buckling behavior of cylindrical shells under external loading conditions. In line with the established research conducted by Hunt *et al.* (1986), Gonçalves and Batista (1988), and Gonçalves and Prado (2002), the transverse deformations of cylindrical shells can be expressed as a function of applied loads and inherent structural characteristics.

$$w(x) = W_0 + W_1 \sin \alpha x \sin \beta y + W_2 \sin^2 \alpha x \quad (39)$$

in which  $\alpha = \frac{m\pi}{L}$  and  $\beta = \frac{n}{R}$ . By inserting the last relation in Eq. (35), the compatibility comparison achieved as Eqs. (40) and (41).

The common solution of  $\Psi(x,y)$  can be achieved from Eq. (41), which is presented in the form of Eq. (42) as:

$$\begin{aligned} \Psi(x, y) &= \Psi_1 \cos(\beta y + \alpha x) + \Psi_2 \cos(\beta y - \alpha x) \\ &+ \Psi_3 \cos(2\beta y + 2\alpha x) + \Psi_4 \cos(2\alpha x - 2\beta y) \\ &+ \Psi_5 \cos(3\alpha x + \beta y) + \Psi_6 \cos(3\alpha x - \beta y) \\ &+ \Psi_7 \cos(\alpha x) + \Psi_8 \end{aligned} \quad (42)$$

in which  $\Psi_i, i = 1, 2, \dots, 8$  remain known coefficients which are achieved by substituting the answer of Eq. (42) in Eq. (41).

Replacing  $\Psi(x, y)$  using the Eq. (42) in Eq. (36), the

$$\begin{aligned}
 & \left[ A_{11}^* \frac{\partial^4 \Psi}{\partial x^4} + (A_{12}^* + A_{21}^* + A_{66}^*) \frac{\partial^4 \Psi}{\partial x^2 \partial y^2} + A_{22}^* \frac{\partial^4 \Psi}{\partial y^4} \right] \\
 & - B_{11}^* \alpha^4 \left[ W_1 \sin(\alpha x) \sin(\beta y) + 8W_2 \sin^2(\alpha x) - 8W_2 \cos^2(\alpha x) \right] \\
 & - (B_{12}^* + B_{21}^* - B_{66}^*) W_1 \alpha^2 \beta^2 \sin(\alpha x) \sin(\beta y) - B_{22}^* \beta^4 \sin(\alpha x) \sin(\beta y) \\
 & = W_1^2 \alpha^2 \beta^2 \cos^2(\alpha x) \cos^2(\beta y) - \frac{\alpha^2}{R} \left[ W_1 \sin(\alpha x) \sin(\beta y) + 2W_2 \cos^2(\alpha x) - 2W_2 \sin^2(\alpha x) \right] \\
 & + \beta^2 \alpha^2 \left[ W_1 \sin(\alpha x) \sin(\beta y) + 2W_2 \cos^2(\alpha x) - 2W_2 \sin^2(\alpha x) \right] W_1 \sin(\alpha x) \sin(\beta y)
 \end{aligned} \tag{40}$$

$$\begin{aligned}
 & A_{11}^* \frac{\partial^4 \Psi}{\partial x^4} + (A_{12}^* + A_{21}^* + A_{66}^*) \frac{\partial^4 \Psi}{\partial x^2 \partial y^2} + A_{22}^* \frac{\partial^4 \Psi}{\partial y^4} \\
 & = \frac{1}{4} W_1^2 \alpha^2 \beta^2 [\cos(2\alpha x - 2\beta y) + \cos(2\alpha x + 2\beta y)] - \frac{1}{2} W_1 W_2 \alpha^2 \beta^2 \cos(3\alpha x - \beta y) \\
 & - \frac{W_1}{2R} ([B_{11}^* \alpha^4 + \beta^2 (B_{12}^* + B_{21}^* - B_{66}^* + W_2) \alpha^2 + B_{22}^* \beta^4] R - \alpha^2) [\cos(\alpha x - \beta y) + \cos(\alpha x + \beta y)] \\
 & + \frac{1}{2} W_1 W_2 \alpha^2 \beta^2 \cos(3\alpha x + \beta y) + \frac{\alpha^2}{2R} (4W_2 - 16RB_{11}^* W_2 \alpha^2) \cos(\alpha x) - \frac{1}{4} W_1^2 \alpha^2 \beta^2
 \end{aligned} \tag{41}$$

energy of structure can be achieved in terms of  $W_0$ ,  $W_1$  and  $W_2$ . To compute these variables, we utilize the Ritz energy method, a powerful technique in variational calculus that allows for the approximation of complex structural behaviors. This method is particularly effective for analyzing the buckling and post-buckling behavior of structures, such as cylindrical shells with lattice cores and nanocomposite surface layers.

$$\frac{\partial U_{TPE}}{\partial W_0} = \frac{\partial U_{TPE}}{\partial W_1} = \frac{\partial U_{TPE}}{\partial W_2} = 0 \tag{43}$$

By the above relationships, an algebraic equation system of three equations with three unknown constants of  $W_0$ ,  $W_1$  and  $W_2$  are obtained.

By Eq. (42) and introducing Eq. (36) into Eq. (43), we will have:

$$\begin{aligned}
 & \frac{\partial U_{TPE}}{\partial W_0} = 4K_4(2W_0 + W_2) \\
 & + \frac{\pi L}{2A_{11}^* R} \times \left[ 4A_{11}^* (A_{12}^* + K_5) \sigma_{0x} h \right. \\
 & \left. - 4A_{11}^* q R - K_4 (W_1^2 \beta - 8A_{12}^* \sigma_{0x} h) \right] = 0
 \end{aligned} \tag{44}$$

Lastly, considering the second two terms of Eq. (43) and considering  $W_1 \neq 0$ , we will have:

$$W_1^2 = - \frac{H_1 + H_2 W_2^2 + H_3 W_2 - 0.5 \alpha^2 \sigma_{0x} h}{H_4} \tag{45}$$

$$q = H_5 W_2 + H_6 W_1^2 + H_7 W_1^2 W_2 - 0.5 W_2 \sigma_{0x} h \tag{46}$$

in which  $H_i, i = 1, 2, \dots, 7$  remain unknown coefficients. By Eqs. (45) and (46), we will have:

$$\begin{aligned}
 & \sigma_{0x} = \frac{2}{[H_6 + (H_7 - 2H_2)W_2] \alpha^2} \times \\
 & \left[ \begin{aligned} & H_1 H_6 + H_3 q \\ & + (H_1 H_7 + H_4 H_6 - H_2 H_5) W_2 \\ & + (H_3 H_6 + H_5 H_7 + H_3 H_7 f) W_2^2 \end{aligned} \right]
 \end{aligned} \tag{47}$$

Ignoring the nonlinear buckling mode shape in Eq. (47),  $W_2 = 0$ , Eq. (47) becomes:

$$\sigma_{0x} = \frac{2H_1}{\alpha^2} + \frac{H_3 q}{H_6 \alpha^2} \tag{48}$$

Using the aforementioned approach, we can derive the relationship between the linear buckling load and the axial stress acting on the cylindrical shell. This relationship is fundamental in understanding how external loads influence the stability of the structure. If  $q = 0$ , then we will have:

$$\begin{aligned}
 & \sigma_{0x} h = \frac{1}{A_{11}} \frac{A_{11}^2 - A_{12}^2}{R^2} \times \left( \frac{\alpha}{\alpha^2 + \beta^2} \right)^2 \\
 & + (A_{11} A_{21} - B_{11}^2) \times \left( \frac{\alpha}{\alpha^2 + \beta^2} \right)^2 + \frac{2(A_{12} B_{11} - A_{11} B_{12})}{R}
 \end{aligned} \tag{49}$$

By Eq. (49), it is possible to achieve the value of the buckling load, which is corresponding to the minimum rate achieved for values of  $n$  and  $m$ .

If  $\sigma_{0x} = 0$ , then the critical compressive load for the sandwich shell strengthened with GPLs is obtained as:

$$\begin{aligned}
 & q = \frac{2\beta^2}{C_2 R^3 (\alpha^4 + \beta^4) (\alpha^2 + \beta^2)^2} \times \\
 & [C_2 (9\alpha^2 + 2\alpha^2 \beta^2 + \beta^4) - 12C_1 R \alpha^2 (\alpha^2 + \beta^2)^2] \\
 & \times \left[ \begin{aligned} & C_2^2 K_4 \alpha^4 - 2C_1 C_2 K_4 R \alpha^2 (\alpha^2 + \beta^2)^2 \\ & + (K_1 + C_1^2 K_4) R^2 (\alpha^4 + \beta^4) \end{aligned} \right]
 \end{aligned} \tag{50}$$

Additionally, the average length change of the cylindrical shell under investigation can be expressed mathematically to quantify its deformation due to external loading. This length change is an important parameter in assessing the structural integrity and performance of the shell during operation. The average length change  $\Delta x$  of the cylindrical shell can be calculated using the following relationship:

$$\begin{aligned}\bar{\Delta}x &= -\frac{1}{2\pi RL} \int_0^{2\pi R} \int_0^L u_{,x} dx dy \\ &= -\frac{1}{2\pi RL} \int_0^{2\pi R} \int_0^L \left[ \begin{array}{l} A_{11}\Psi_{,yy} - A_{12}\Psi_{,xx} - B_{11}^*w_{,xx} \\ -B_{12}^*w_{,yy} - 0.5w_{,x}^2 \\ +B_{22}^*(\Phi_{1,x} + w_{,xx}) \end{array} \right] dx dy\end{aligned}\quad (51)$$

Therefore, by replacing Eqs. (39) and (42) into Eq. (51), the length change of the cylindrical shell is obtained.

#### 4. Results and discussions

In this section, the buckling load and post-buckling paths of sandwich cylinder-shaped shell to lattice core and top reinforced with GPLs are discussed. The analytical solutions were obtained using MATLAB software, which provided the necessary computational capabilities to handle the numerous equations and matrices involved in the analysis. Material specifications include: core:  $E_c = 2400\text{MPa}$ ,  $\rho_c = 1180 \frac{\text{kg}}{\text{m}^3}$  and  $\nu_c = 0.35$ . Surface layer matrix:  $E_m = 1.3 \times 10^5\text{MPa}$ ,  $\rho_m = 8960 \frac{\text{kg}}{\text{m}^3}$  and  $\nu_m = 0.34$ . GPL (Liu *et al.* 2007):  $l_{GPL} = 2.5\mu\text{m}$ ,  $h_{GPL} = 1.5\text{nm}$ ,  $w_{GPL} = 1.5\mu\text{m}$ ,  $E_{GPL} = 1.01\text{TPa}$ ,  $\rho_{GPL} = 1060.5 \frac{\text{kg}}{\text{m}^3}$ , and  $\nu_{GPL} = 0.186$ .

##### 4.1 Verification

The post-buckling equilibrium paths of the cylinder-shaped shell reinforced with uniformly distributed GPLs are shown in Fig. 3 with the analytical results of Huang and Han (2009) to verify the accuracy of the technique used in this work regardless of the thickness of the lattice core. According to the present research, the post-buckling path achieved is in reasonable agreement with the published results in both pre-buckling and post-buckling areas. The bifurcation point and buckling paths in Fig. 3 differ slightly (less than 2%) due to the different theories employed.

The multi-valued dependence of stress on length shortening, as observed in Fig. 3 and other related figures, is indicative of the complex buckling behavior exhibited by the structure under compressive loading. This phenomenon reflects the presence of multiple equilibrium states that the structure can adopt during the buckling process, resulting from non-linear geometric effects. Such behavior is characteristic of softening mechanisms in materials and can lead to post-buckling stability challenges. This aspect is crucial for understanding the performance of nano-composites in practical applications, where such instability could affect their load-bearing capacity and overall reliability.

The current findings regarding the linear buckling load of functionally graded carbon nanotube (FG-CNT) reinforced cylindrical shells are summarized in Table 1, where they are compared with the results reported by Torabi *et al.* (2019) in a related study. This comparison serves to validate the accuracy and reliability of the proposed model. As evident from the table, there is a notable alignment between our results and those presented by Torabi *et al.*

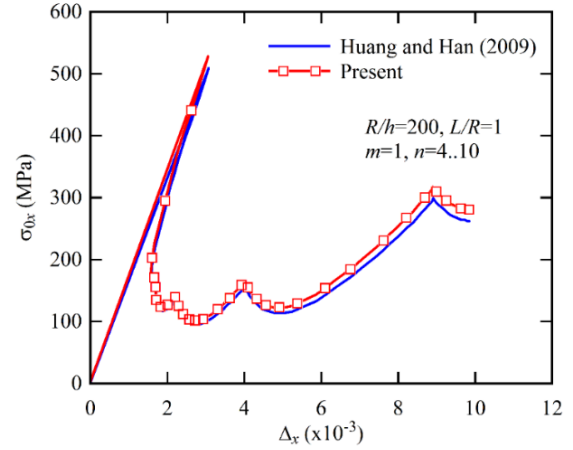


Fig. 3 Post-buckling track of simply supported isotropic cylinder-shaped shell

Table 1 Linear and nonlinear buckling load of simply supported FG-GPL reinforced cylinder-shaped shell ( $L/R=1.5$ ,  $R/h=100$ )

$W_{GPL}$	Linear		Nonlinear	
	Present study	Torabi <i>et al.</i> (2019)	Present study	Torabi <i>et al.</i> (2019)
0.5	398.72	392.24	315.67	311.17
1	546.03	539.91	511.34	506.31
2	1131.82	1125.83	903.71	898.08

(2019), indicating that the model developed in this research accurately captures the essential mechanics of FG-CNT reinforced cylindrical shells under buckling conditions. The close correspondence between the values not only reinforces the credibility of the analytical approach utilized in this study but also highlights the effectiveness of FG-CNT reinforcements in enhancing the buckling resistance of cylindrical structures. This agreement is crucial for establishing confidence in the predictive capabilities of the model, ensuring its applicability for future investigations and design considerations in engineering applications involving composite materials.

##### 4.2 Nonlinear buckling behavior

Eq. (47) can be applied to calculate the nonlinear buckling loads that result from large deformations of the cylindrical shell under study. Since algebraic equations are nonlinear, to define the critical conditions, the axial stress curve is drawn according to  $W_2$  and the lowest point is deliberated the nonlinear buckling condition. To define the critical conditions of a structure, the following procedure is followed: For a certain value of  $q$ , variation are drawn in terms of  $W_2$  and in the form of a certain mode ( $n, m$ ), and from these curves, the critical axial stress  $\sigma_{cr}$  is calculated for each specific mode (Fig. 4a). In Fig. 4b, the curve of changes  $q$  is drawn with  $W_2$  using a specific value of  $\sigma_{0x}$ , and based on these curves, it is possible to determine the critical radial pressure,  $q_{cr}$ , corresponding to the mode of ( $n, m$ ) at the minimum point of each curve. Based on the

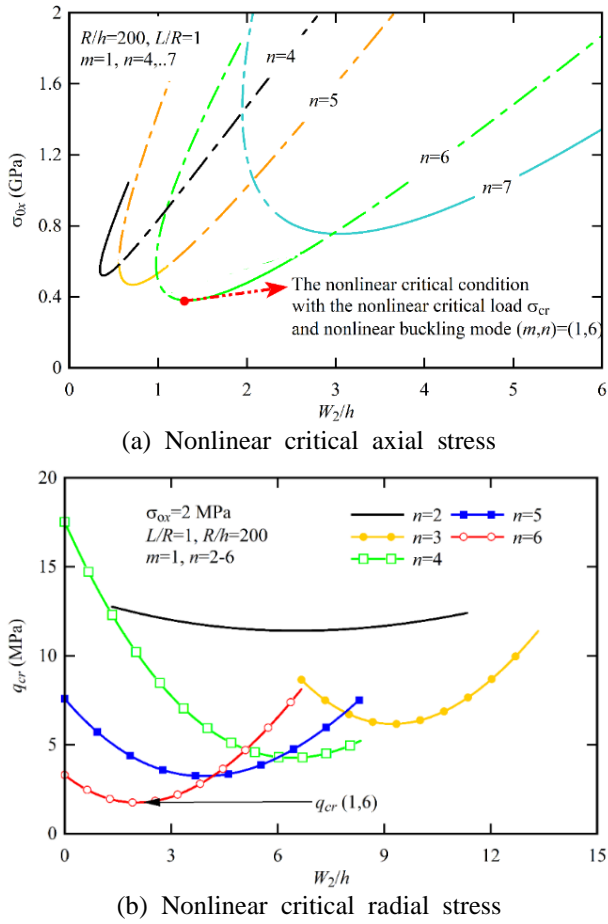


Fig. 4 Determining the critical buckling conditions of the cylindrical shell

curves shown in Fig. 4, it can be seen that for a uniform distribution of nanoparticles, the critical axial stress and critical radial pressure of the configuration are 0.39 GPa and 1.73 MPa, respectively.

For different distributions of GPLs, GPLs weight fractions (wt%), and core-to-layer thickness ratios, Table 2 illustrates the lowest critical stress of the sandwich shell under lateral pressure of 100 kPa. According to Table 1, for all modes of GPLs distribution, the addition of a very small quantity of GPLs significantly increases the equivalent stiffness of the structure. The findings indicate a substantial enhancement in the maximum critical stress of the sandwich shell structures under investigation. Specifically, the addition of GPLs demonstrates varying impacts depending on their distribution mode; the GPL-S mode exhibits the least influence, whereas the GPL-A mode shows the most significant enhancement. Furthermore, the analysis reveals that increasing the ratio of core thickness to surface layer thickness leads to a marked increase in maximum critical stress. This is attributed to the fact that a thicker lattice core enhances the bending strength of the shell, thereby resulting in a higher buckling load and an increase in maximum critical stress. Notably, in the case of the GPL-A sandwich shell configuration, the critical axial stress experiences an approximate 6.7 increase when the thickness ratio escalates from 0.0 to 4. This trend underscores the critical role of

Table 2 Effect of lattice core on serious axial stress (GPa) for different states of GPLs distribution ( $\alpha_x = \alpha_y = 4, \beta = 0.1, \frac{L}{R} = 2, \frac{R}{h} = 200, q = 0.1\text{MPa}$ )

	$W_{GPL}$	$h_c/h_f$			
		0	2	4	6
GPL-U	0.1	0.18	1.05	1.38	2.45
	0.2	0.25	1.47	1.64	2.68
	0.4	0.38	1.89	2.08	3.13
	0.5	0.63	2.38	2.61	3.63
GPL-S	0.1	0.13	0.83	1.24	2.17
	0.2	0.19	1.25	1.51	2.35
	0.4	0.25	1.57	1.84	2.91
	0.5	0.52	1.98	2.31	3.47
GPL-A	0.1	0.23	1.19	1.79	2.96
	0.2	0.31	1.66	2.13	3.20
	0.4	0.45	2.14	2.46	3.68
	0.5	0.78	2.63	3.19	4.07
-	0	0.05	0.67	1.06	1.78

Table 3 Effect of lattice core on critical radial pressure (MPa) of cylindrical shell reinforced with GPLs for different modes of GPLs distribution ( $\alpha_x = \alpha_y = 4, \beta = 0.1, \frac{L}{R} = 2, \frac{R}{h} = 200, \sigma_{0x} = 50\text{MPa}$ )

	$W_{GPL}$	$h_c/h_f$			
		0	2	4	6
GPL-U	0.1	0.57	4.25	6.04	9.35
	0.2	0.81	6.57	7.61	11.22
	0.4	1.28	8.24	10.57	14.19
	0.5	2.29	10.80	13.04	17.07
GPL-S	0.1	0.41	3.18	5.26	7.22
	0.2	0.61	5.31	6.81	8.57
	0.4	0.81	7.17	8.91	10.20
	0.5	1.83	9.86	12.27	14.45
GPL-A	0.1	0.74	4.57	7.57	12.64
	0.2	1.03	7.11	8.93	14.80
	0.4	2.55	9.82	11.37	17.58
	0.5	3.35	12.67	14.95	20.77
-	0	0.35	3.46	5.30	8.51

core thickness in optimizing the structural integrity of sandwich shells. Table 3 corroborates these observations, illustrating that the critical radial pressure—responsible for inducing buckling—also shows significant improvement due to the inclusion of mesh cores. The data presented in this table clearly demonstrates that the implementation of lattice structures markedly enhances the critical radial pressure capacity of the sandwich shells, affirming their potential in advanced engineering applications. Compared to the unreinforced sample, the GPL-A mode and for  $h_c/h_f=4$  causes an increase of about 5.7 times the critical radial pressure for 0.2%.

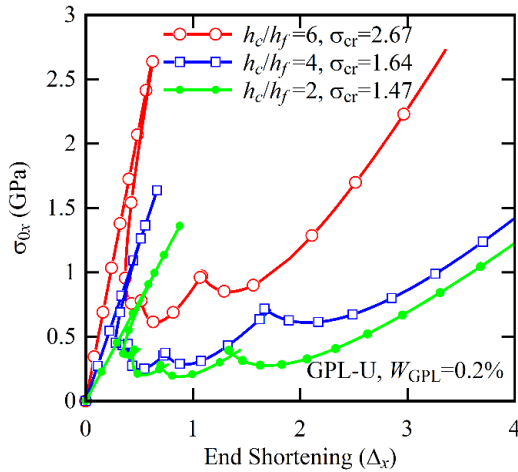


Fig. 5 Effect of lattice core thickness on post-buckling path of cylinder-shaped shell with lattice core and GPL strengthened surface layer

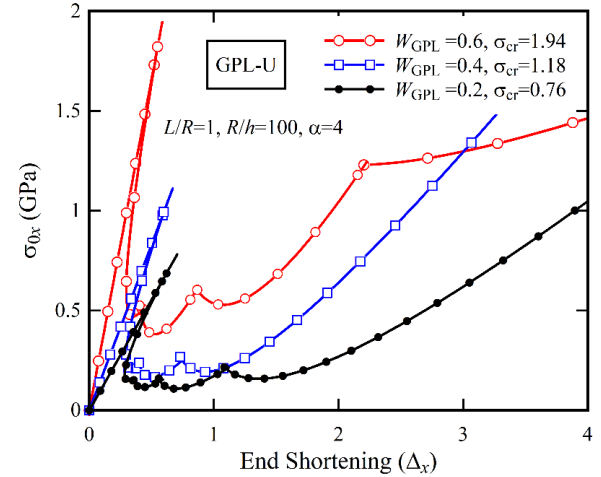


Fig. 7 The influence of weight fraction of GPLs on post-buckling performance curve of the cylinder-shaped sandwich shell

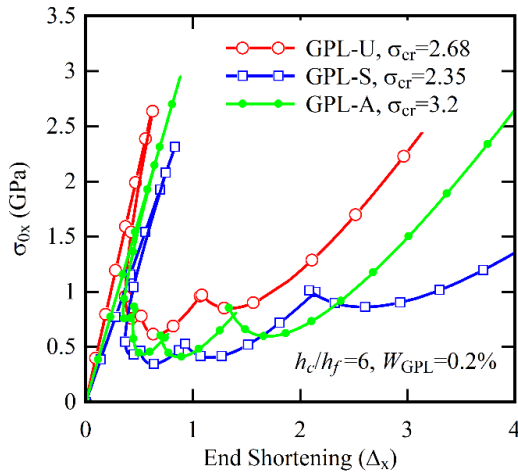


Fig. 6 Influence of GPL distribution type on post-buckling performance of cylinder-shaped shell with lattice core and GPL strengthened surface layer

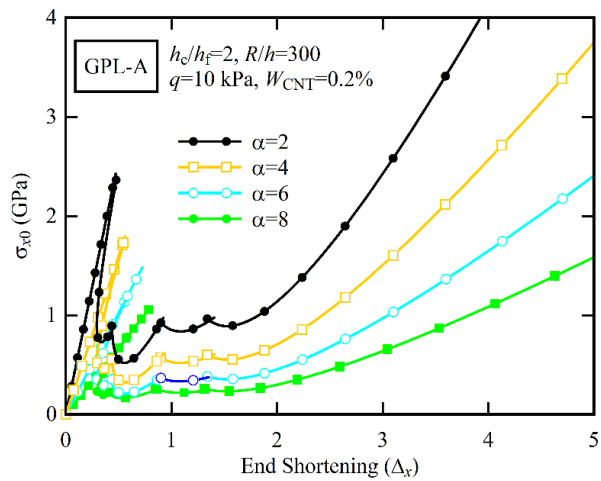


Fig. 8 Effect of the geometrical parameter of lattice core on post-buckling behavior curve of the cylinder-shaped sandwich shell

### 4.3 Post-buckling behavior

In Fig. 5, thickness ratio of lattice core to the layers is shown in relation to the length variation of the cylinder-shaped sandwich shell and its critical axial stress. Results show that equilibrium path of post-buckling behavior rises with increasing lattice core thickness, which is caused by an increase in equivalent bending strength of the configuration due to the lattice core. Fig. 6 illustrates the influence of GPL distribution type on the post-buckling performance of a sandwich shell. As seen from the Fig. 6, the distribution of GPLs affects the initial stiffness (slope of force-displacement curve) of the structure. It should be noted that, unlike the stiffness, the maximum critical radial pressure is obtained for the non-uniform distribution of GPL-A. The non-uniform distribution of GPL-A, however, results in the highest critical radial pressure, as opposed to the stiffness. Because of the significant influence of GPL distribution type on stiffness of the structure, the ductility is also

modified, and the critical end-shortening ratio of the shell is 0.61, 0.84, and 0.89, respectively, for GPL-U, GPL-S, and GPL-A states. Therefore, the distribution method of GPL has a different impact on the initial stiffness, critical radial pressure, and end-shortening ratio of the shell under study, and the appropriate distribution method can be selected according to the application.

The buckling behavior curve for GPL-U distribution mode is shown in Fig. 7, which shows the impact of the weight fraction of GPLs and the geometric characteristics of lattice core on the buckling performance of cylindrical sandwich shells. As can be seen from the results, as the weight fraction increases, hardening behavior occurs in the system, resulting in an increase in the quantity of force essential to generate a displacement in sandwich cylinder. To create a 0.2 end-shortening ratio, and weight fractions of GPL of 0.2, 0.4, and 0.6 wt.% the critical axial stress obtained as 0.24 GPa, 0.33 GPa and 0.66 GPa, respectively. Furthermore, as can be seen, even though the added GPLs

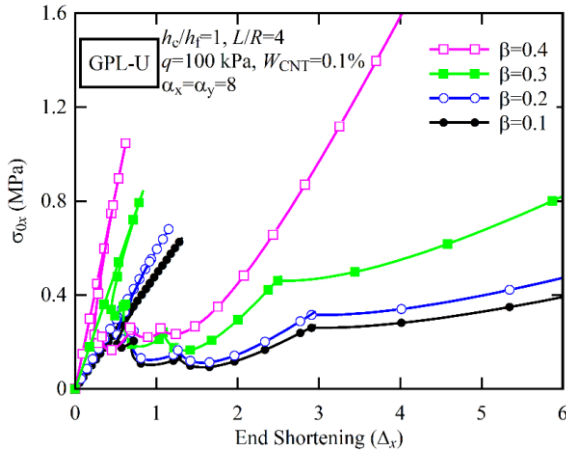


Fig. 9 The impact of the cellular thickness ratio on the post-buckling performance curve of the cylinder-shaped sandwich shell

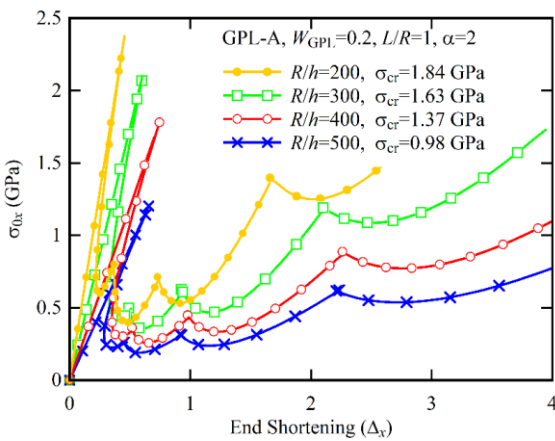


Fig. 10 The effect of  $R/h$  ratio on the post-buckling performance curve of cylindrical sandwich shell

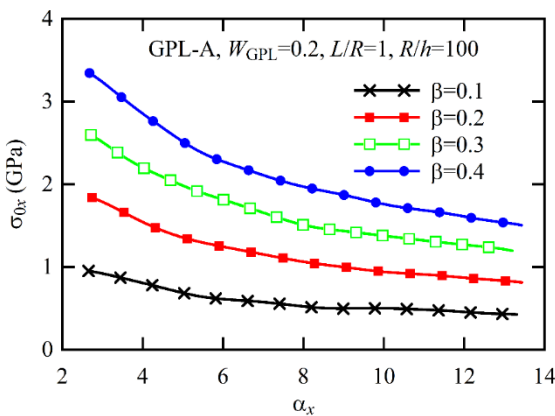


Fig. 11 The effect of the geometric features of the lattice core on critical axial stress of cylindrical sandwich shell.

increase the critical buckling load of the system, the extreme movement required to cause buckling reductions as the stiffness increases equivalent to the added weight fraction. As shown in Fig. 8, the effect of the lattice core dimension coefficient i.e.,  $\alpha_x$  is opposite to the weight

fraction of the GPL, i.e., with increase of lattice core coefficient, the critical buckling stress reductions while the end-shortening ratio required to buckling rises. Therefore, with collective  $\alpha_x$ , the effective elastic modulus of the core decreases, causing the material to exhibit softening behavior. Similarly, Fig. 9 illustrates the effect of the dimensionless thickness of lattice core cells,  $\beta$ , on the mechanical performance of sandwich shell. By cumulative  $\beta$ , the stiffness of the structure increases its bending resistance, which in turn increases the critical axial force. The  $R/h$  ratio is another parameter that affects the buckling performance of strengthened cylinder-shaped shells for GPL-A distribution mode. Fig. 10 illustrates the influence of these constraints on post-buckling behavior.

Fig. 11 shows the influence of cell wall thickness fraction of the reticular core,  $\beta$ , and the cell length ratio,  $\alpha_x$ , on critical stress of cylinder-shaped sandwich shell. As these results show, the increase of  $\alpha_x$  causes a decrease in the critical stress of the cylinder-shaped shell, which occurs as a result of a decrease in the elastic modulus and the corresponding stiffness of shell. For example for  $\beta = 0.1$  and  $\beta = 0.4$ , by increasing  $\alpha_x$  from 4 to 8, the critical axial stress decreases by 35% and 32%, respectively. In addition, increasing thickness of cell wall increases the critical buckling stress.

### 5. Conclusions

This study examined the nonlinear buckling and post-buckling performance of sandwich cylindrical shells with lattice cores and GPLs reinforced surface layers. The Ritz energy technique was used to extract explicit relationships between axial force and critical radial pressure. A study was conducted to examine the effects of various parameters, including the type of GPLs distribution, GPLs volume fraction, and the geometric characteristics of the lattice core and shell, on the buckling and post-buckling behavior of these shells.

- Based on the results, lattice cores significantly enhance the carrying capacity of sandwich shells and can increase it by up to 6.7 times when compared to shells without lattice cores.

- GPLs and their distribution affect the buckling behavior of the shells, and a minimal amount of GPLs can cause a significant increase in buckling characteristics, and the critical buckling stress can increase by approximately 65%.

- In this study, we observed a notable enhancement in structural strength, with an improvement of 65% compared to baseline models. This improvement can be attributed to the optimized design of the nanocomposite structure, which effectively utilizes the unique mechanical properties of the nanoscale materials. The methodologies employed, including analytical method, allowed for precise measurements and validation of our findings.

- These results indicate a significant potential for practical applications in lattice core and graphene platelet-reinforced surfaces, underscoring the relevance of this research in advancing nanocomposite technology.

## References

- Abbandanak, S.N.H., M.H. Siadati and R. Eslami-Farsani (2018), "Effects of functionalized graphene nanoplatelets on the flexural behaviors of basalt fibers/epoxy composites", *J. Compos. Sci.*, **5**(3), 315-324.
- Akbarzadeh, I., A.S. Poor, M. Khodarahmi, M. Abdihaji, A. Moammeri, S. Jafari, Z.S. Moghaddam, M. Seif, M. Moghtaderi and Z.A. Lalami (2022), "Gingerol/tetrazole-loaded mesoporous silica nanoparticles for breast cancer therapy: In-silico and in-vitro studies", *Micropor. Mesopor. Mater.*, **337**, 111919. <https://doi.org/10.1016/j.micromeso.2022.111919>.
- An, Q., M. Bagheritabar, A. Basem, A.A. Ghabra, Y. Li, M. Tang, L.S. Sabri and R. Sabetvand (2024), "The effect of size of copper oxide nanoparticles on the atomic and thermal behavior of silica aerogel/paraffin nanostructure in a cylindrical duct using molecular dynamics simulation", *Case Stud. Therm. Eng.*, **104666**. <https://doi.org/10.1016/j.csite.2024.104666>.
- Bhandari, S. (2019), *Polymer/Carbon Composites for Sensor Application. Springer Series on Polymer and Composite Materials*, Springer, Singapore. [https://doi.org/10.1007/978-981-13-2688-2\\_14](https://doi.org/10.1007/978-981-13-2688-2_14).
- Boroujeni, F.M., G. Fioravanti and R. Kander (2024), "Synthesis and characterization of cellulose microfibril-reinforced polyvinyl alcohol biodegradable composites", *Materials*, **17**(2), 526. <https://doi.org/10.3390/ma17020526>.
- Celiktas, M.S., M. Yaglikci and F.K. Maleki (2019), "Subcritical water extraction derived lignin for creation of sustainable reinforced composite materials", *Polym. Test.*, **77**, 105918. <https://doi.org/10.1016/j.polymertesting.2019.105918>.
- Chen, Y., F. Scarpa, Y. Liu and J. Leng (2013), "Elasticity of anti-tetrachiral anisotropic lattices", *Int. J. Solids Struct.*, **50**(6), 996-1004. <https://doi.org/10.1016/j.ijsolstr.2012.12.004>.
- Duc, N.D., K. Seung-Eock, P.H. Cong, N.T. Anh and N.D. Khoa (2017), "Dynamic response and vibration of composite double curved shallow shells with negative Poisson's ratio in auxetic honeycombs core layer on elastic foundations subjected to blast and damping loads", *Int. J. Mech. Sci.*, **133**, 504-512. <https://doi.org/10.1016/j.ijmecsci.2017.09.009>.
- Faraji, A., A.R. Farahani, N.B. Khoramdareh, A. Gil, S. Jafari, Z. Hekmatian and N. Shojaei (2023), "Cu-Fe nanoparticles decorated rice hull/chitosan@ FeAl<sub>2</sub>O<sub>4</sub> to boosted peroxidase-like activity for catalytic degradation of antibiotics: Kinetics and mechanistic insights", *J. Environ. Chem. Eng.*, **11**(6), 111348. <https://doi.org/10.1016/j.jece.2023.111348>.
- Faraji, A., N.B. Khoramdareh, F. Falahati, S. Jafari, S.A. Monfared and A. Faghieh (2023), "Superparamagnetic MnFe alloy composite derived from cross-bindered of chitosan/rice husk waste/iron aluminate spinel hercynite for rapid catalytic detoxification of aflatoxin B1: Structure, performance and synergistic mechanism", *Int. J. Biol. Macromol.*, **234**, 123709. <https://doi.org/10.1016/j.ijbiomac.2023.123709>.
- Feng, C., S. Kitiipornchai and J. Yan (2017), "Nonlinear bending of polymer nanocomposite beams reinforced with non-uniformly distributed graphene platelets (GPLs)", *Compos. B. Eng.*, **110**, 132-140. <https://doi.org/10.1016/j.compositesb.2016.11.024>.
- Gonçalves, P. and R. Batista (1988), "Non-linear vibration analysis of fluid-filled cylindrical shells", *J. Sound Vib.*, **127**(1), 133-143. [https://doi.org/10.1016/0022-460X\(88\)90354-9](https://doi.org/10.1016/0022-460X(88)90354-9).
- Gonçalves, P.B. and Z.J. Del Prado, (2002), "Nonlinear oscillations and stability of parametrically excited cylindrical shells", *Meccanica*, **37**(6), 569-597. <https://doi.org/10.1023/A:1020972109600>.
- Hao, Y., A. Basem, M. Bagheritabar, D.J. Jasim, B. Keivani, A. H. Kareem, A.J. Sultan, S. Salahshour and S. Esmaeili (2024), "The computational study of silicon doping and atomic defect influences on the CNT's nano-pumping process: Molecular dynamics approach", *Int. Commun. Heat and Mass Transf.*, **152**, 107302. <https://doi.org/10.1016/j.icheatmasstransfer.2024.107302>.
- Huang, H. and Q. Han (2009), "Nonlinear elastic buckling and postbuckling of axially compressed functionally graded cylindrical shells", *Int. J. Mech. Sci.*, **51**(7), 500-507. <https://doi.org/10.1016/j.ijmecsci.2009.05.002>.
- Hunt, G.W., K. Williams and R. Cowell (1986), "Hidden symmetry concepts in the elastic buckling of axially-loaded cylinders", *Int. J. Solids Struct.*, **22**(12), 1501-1515. [https://doi.org/10.1016/0020-7683\(86\)90058-2](https://doi.org/10.1016/0020-7683(86)90058-2).
- Jahanghri, R., R. Yahyazadeh, N. Sharafkhani and V.A. Maleki (2016), "Stability analysis of FGM microgripper subjected to nonlinear electrostatic and temperature variation loadings", *Sci. Eng. Compos. Mater.*, **23**(2), 199-207. <https://doi.org/10.1515/secm-2014-0079>.
- Javani, M., Y. Kiani and M. Eslami (2021), "Geometrically nonlinear free vibration of FG-GPLRC circular plate on the nonlinear elastic foundation", *Compos. Struct.*, **261**, 113515. <https://doi.org/10.1016/j.compstruct.2020.113515>.
- Karami, B., D. Shahsavari, M. Janghorban and A. Tounsi (2019), "Resonance behavior of functionally graded polymer composite nanoplates reinforced with graphene nanoplatelets", *Int. J. Mech. Sci.*, **156**, 94-105. <https://doi.org/10.1016/j.ijmecsci.2019.03.036>.
- Karnesis, N. and G. Burriesci (2013), "Uniaxial and buckling mechanical response of auxetic cellular tubes", *Smart. Mater. Struct.*, **22**(8), 084008. <https://doi.org/10.1088/0964-1726/22/8/084008>.
- Khosravi, S., Yousefi, M.M. and Goudarzi, M. (2021), "Development of seismic fragility curves of cylindrical concrete tanks using nonlinear analysis", *Amirkabir J. Civil Eng.*, **53**(1), 71-88. <https://doi.org/10.22060/ceej.2021.19121.7079>.
- Kim, J. and J. Reddy (2015), "A general third-order theory of functionally graded plates with modified couple stress effect and the von Kármán nonlinearity: theory and finite element analysis", *Acta Mechanica*, **226**(9), 2973-2998. <https://doi.org/10.1007/s00707-015-1370-y>.
- Kolahdouzan, F., Mosayyebi, M., Ghasemi, F.A., Kolahchi, R. and Panah, S.R.M., (2020) "Free vibration and buckling analysis of elastically restrained FG-CNTRC sandwich annular nanoplates", *Adv. Nano Res.*, **9**(4), 237-250. <https://doi.org/10.12989/anr.2020.9.4.237>.
- Lakes, R. (1991), "Deformation mechanisms in negative Poisson's ratio materials: Structural aspects", *J. Mater. Sci.*, **26**, 2287-2292. <https://doi.org/10.1007/BF01130170>.
- Lei, Z., L. Zhang, K. Liew and J. Yu (2014), "Dynamic stability analysis of carbon nanotube-reinforced functionally graded cylindrical panels using the element-free kp-Ritz method", *Compos. Struct.*, **113**, 328-338. <https://doi.org/10.1016/j.compstruct.2014.03.035>.
- Li, C., H.S. Shen and H. Wang (2019), "Thermal post-buckling of sandwich beams with functionally graded negative Poisson's ratio honeycomb core", *Int. J. Mech. Sci.*, **152**, 289-297. <https://doi.org/10.1016/j.ijmecsci.2019.01.002>.
- Li, C., H.S. Shen and H. Wang (2020), "Postbuckling behavior of sandwich plates with functionally graded auxetic 3D lattice core", *Compos. Struct.*, **237**, 111894. <https://doi.org/10.1016/j.compstruct.2020.111894>.
- Li, C., J. Yang and H.S. Shen (2022), "Postbuckling of pressure-loaded auxetic sandwich cylindrical shells with FG-GRC facesheets and 3D double-V meta-lattice core", *Thin Wall. Struct.*, **177**, 109440. <https://doi.org/10.1016/j.tws.2022.109440>.
- Lim, T.C. (2014a), "Buckling and vibration of circular auxetic plates", *J. Eng. Mater. Technol.*, **136**(2), 56-70. <https://doi.org/10.1115/1.4026617>.

- Lim, T.C. (2014b), "Elastic stability of thick auxetic plates", *Smart. Mater. Struct.*, **23**(4), 045004.  
<https://doi.org/10.1088/0964-1726/23/4/045004>.
- Pourreza, T., A. Alijani, V.A. Maleki and A. Kazemi (2021), "Nonlinear vibration of nanosheets subjected to electromagnetic fields and electrical current", *Adv. Nano Res.*, **10**(5), 481-491.  
<https://doi.org/10.12989/anr.2021.10.5.481>.
- Pourreza, T., A. Alijani, V.A. Maleki and A. Kazemi (2022), "The effect of magnetic field on buckling and nonlinear vibrations of Graphene nanosheets based on nonlocal elasticity theory", *Int. J. Nano Dimension*, **13**(1), 54-70.  
<https://doi.org/10.22034/ijnd.2022.683988>.
- Pozniak, A. and K. Wojciechowski (2014), "Poisson's ratio of rectangular anti-chiral structures with size dispersion of circular nodes", *Physica Status Solidi B*, **251**(2), 367-374.  
<https://doi.org/10.1002/pssb.201384256>.
- Pozniak, A., J. Smardzewski and K. Wojciechowski (2013), "Computer simulations of auxetic foams in two dimensions", *Smart Mater. Struct.*, **22**(8), 084009.  
<https://doi.org/10.1088/0964-1726/22/8/084009>
- Quang, V.D., T.Q. Quan and P. Tran (2022), "Static buckling analysis and geometrical optimization of magneto-electro-elastic sandwich plate with auxetic honeycomb core", *Thin Wall. Struct.*, **173**, 108935.  
<https://doi.org/10.1016/j.tws.2022.108935>.
- Reddy, J. N. (2003), *Mechanics of Laminated Composite Plates and Shells: Theory and Analysis*, CRC press.
- Rezaee, M. and V.A. Maleki (2015), "An analytical solution for vibration analysis of carbon nanotube conveying viscose fluid embedded in visco-elastic medium", *Proceedings of the Institution of Mechanical Engineers, Part C: Journal of Mechanical Engineering Science*, **229**(4), 644-650.  
<https://doi.org/10.1177/0954406214538011>.
- Rostami, N., Ghebleh, A., Noei, H., Rizi, Z.S., Moeinzadeh, A., Nikzad, A., Gomari, M.M., Uversky, V.N. and Tarighi, P., (2024), "Peptide-functionalized polymeric nanoparticles for delivery of curcumin to cancer cells", *J. Drug. Deliv. Sci. Technol.*, **102**, 106337.  
<https://doi.org/10.1016/j.jddst.2024.106337>.
- Scarpa, F., C. Smith, M. Ruzzene and M. Wadee (2008), "Mechanical properties of auxetic tubular truss-like structures," *Phys. Status Solidi B*, **245**(3), 584-590.  
<https://doi.org/10.1002/pssb.200777715>.
- Shah, I.A., R. Khan, S.S.R. Kolor, M. Petrú, S. Badshah, S. Ahmad and M. Amjad (2022), "Finite element analysis of the ballistic impact on auxetic sandwich composite human body armor," *Materials*, **15**(6), 2064-2078.  
<https://doi.org/10.3390/ma15062064>.
- Shi, Z., X. Yao, F. Pang and Q. Wang (2017), "An exact solution for the free-vibration analysis of functionally graded carbon-nanotube-reinforced composite beams with arbitrary boundary conditions," *Sci. Rep.*, **7**(1), 129-140.  
<https://doi.org/10.1038/s41598-017-12596-w>.
- Soleimani-Javid, Z., Arshid, E., Khorasani, M., Amir, S. and Tounsi, A. (2021), "Size-dependent flexoelectricity-based vibration characteristics of honeycomb sandwich plates with various boundary conditions", *Adv. Nano Res.*, **10**(5), 449-460.  
<https://doi.org/10.12989/anr.2021.10.5.449>.
- Strek, T., H. Jopek, B.T. Maruszewski and M. Nienartowicz (2014), "Computational analysis of sandwich-structured composites with an auxetic phase", *Physica Status Solidi B*, **251**(2), 354-366.  
<https://doi.org/10.1002/pssb.201384250>.
- Torabi, J., R. Ansari and R. Hassani (2019), "Numerical study on the thermal buckling analysis of CNT-reinforced composite plates with different shapes based on the higher-order shear deformation theory", *Eur. J. Mech. A Solids*, **73**, 144-160.  
<https://doi.org/10.1016/j.euromechsol.2018.07.009>.
- Toygarg, M.E., O. Sayman, U. Kemiklioglu, H. Öztürk, Z. Kırıl and F.K. Maleki (2016), "Vibration and buckling analysis of a curved sandwich composite beam with FEM", *Res. Eng. Struct. Mater.*, **2**, 49-59.  
<http://doi.org/10.17515/resm2015.27me0929>.
- Wojciechowski, K. (1987), "Constant thermodynamic tension Monte Carlo studies of elastic properties of a two-dimensional system of hard cyclic hexamers", *Mol. Phys.*, **61**(5), 1247-1258.  
<https://doi.org/10.1080/00268978700101761>.
- Wojciechowski, K. (1989), "Two-dimensional isotropic system with a negative Poisson ratio", *Phys. Lett. A*, **137**(1-2), 60-64.  
[https://doi.org/10.1016/0375-9601\(89\)90971-7](https://doi.org/10.1016/0375-9601(89)90971-7).
- Wojciechowski, K. and A. Branca (1989), "Negative Poisson ratio in a two-dimensional isotropic", *Phys. Lett. A Rev*, **40**, 7222-7225.  
<https://doi.org/10.1103/PhysRevA.40.7222>.
- Wu, Z., Y. Zhang, G. Yao and Z. Yang (2019), "Nonlinear primary and super-harmonic resonances of functionally graded carbon nanotube reinforced composite beams", *Int. J. Mech. Sci.*, **153**, 321-340.  
<https://doi.org/10.1016/j.ijmecsci.2019.02.015>.
- Zhang, Y., X. Li and S. Liu (2016), "Enhancing buckling capacity of a rectangular plate under uniaxial compression by utilizing an auxetic material", *Chinese J. Aeronaut.*, **29**(4), 789-803.  
<https://doi.org/10.1016/j.cja.2016.06.010>.

CC